PAPER

Quasi-coherent fluctuation measurement with the upgraded microwave imaging reflectometer in KSTAR

IOP Publishing Plasma Physics and Controlled Fusion
Plasma Phys. Control. Fusion **60** (2018) 115009 (13pp) https://doi.org/10.1088/1361-6587/aae0b5

Quasi-coherent fluctuation measurement with the upgraded microwave imaging reflectometer in KSTAR

W Lee[1], J Leem[2], D J Lee[3], M J Choi[1], H K Park[3], J A Lee[2], G S Yun[2], T G Kim[4], H Park[4], K W Kim[4] and the KSTAR team

[1] National Fusion Research Institute, Daejeon 34133, Republic of Korea
[2] Pohang University of Science and Technology, Pohang 37673, Republic of Korea
[3] Ulsan National Institute of Science and Technology, Ulsan 44919, Republic of Korea
[4] Kyungpook National University, Daegu 41566, Republic of Korea

E-mail: wclee@nfri.re.kr

Received 6 April 2018, revised 31 August 2018
Accepted for publication 12 September 2018
Published 1 October 2018

Abstract

The microwave imaging reflectometer (MIR) is the leading diagnostic tool for study of density fluctuations in KSTAR. For last three years since 2014, major components such as the multi-frequency probe beam source, multi-channel detector array, signal processing electronic system, data acquisition system, and optical system have been gradually upgraded. In this paper, the detailed system upgrade with test results in the laboratory and/or plasma is given, and analysis results of a distinctive fluctuation structure referred to as the quasi-coherent mode (QCM) measured by the upgraded MIR system for an L-mode discharge are presented. Cross-coherence analysis with multiple channels shows that the QCM is localized in a core region and appears to be driven by electron temperature gradient for the discharge.

Keywords: microwave imaging reflectometer, multi-frequency probe beam source, multi-channel detector array, quasi-coherent mode, coherence analysis

(Some figures may appear in colour only in the online journal)

1. Introduction

The microwave imaging reflectometer (MIR) has been the leading diagnostic tool for study of density fluctuations in KSTAR since the commission in 2012. Representative researches utilizing the MIR system are as follows: using the measured effective (or apparent) poloidal velocities of density fluctuations with multiple poloidal channels [1, 2], $E \times B$ flow velocities were estimated for the plasmas heated by neutral beam injection (NBI) [3]. The spatial and temporal scales of the ion-gyroscale turbulence for the L-mode plasmas heated by NBI were estimated from the time-delayed cross-correlation between signals of the multiple poloidal channels, and compared to the parameters associated with the ion-gyroscale turbulence such as ion temperature gradient mode and trapped electron mode (TEM) [3]. The poloidal wavenumbers of the most unstable modes for the L-mode plasmas were deduced from peak frequencies (determined from cross-coherence spectra) and effective poloidal velocities of fluctuations, and they were compared to those predicted from linear and nonlinear gyrokinetic simulations [4, 5]. Recently, characteristics of quasi-coherent modes (QCMs) known as a kind of TEM [6–14] were investigated for the ohmically heated or electron cyclotron resonant heating (ECH) assisted L-mode plasmas [15].

The KSTAR MIR system has been upgraded for three years from 2014 and clear documentation is necessary for better understanding of the physics results to be followed in the future. Thus, the detailed description of the system upgrade along with the test results in the laboratory and/or plasma is given (section 2) and some of the analysis results of quasi-coherent density fluctuations measured by the upgraded system for an L-mode discharge are illustrated (section 3).

2. Upgrade of the MIR system

2.1. Increase of the radial channels

One of the major upgrade from 2014 is an increase of the radial channels (from two to four of the number of the probing frequencies). Each frequency beam source consists of a phase-locked synthesizer ($f = 13-16$ GHz with 1 MHz steps), ×6 frequency multiplier (Millitech, AMC-10-RNHB0), and power amplifier (Millitech, AMP-10-02440), and it produces a high-power signal of up to +21 dBm in the range from 78 to 96 GHz. Each output frequency can be remotely controlled in-between discharges, and the interval of the probing frequencies is fixed at 1.8 GHz. Note that the interval of two probing frequencies before the upgrade was 4.0 GHz. Four-frequency output signals are combined by two-stage hybrid couplers (Millitech, CMT-10-R6000) and radiated as four-frequency electromagnetic waves through a single Gaussian antenna. The structure of the local oscillator (LO) source is similar with that of the single-frequency probe beam source but different models are used (Millitech AMC-10-RFBH0 for the multiplier and Millitech AMP-10-02290 for the amplifier). Figure 1 shows the schematic layout of the four-frequency probe beam source and LO source, and an actual image of the probe beam source.

Figure 2 shows output spectra of the MIR synthesizer (custom-made by the EM-Wise Communications) compared with those of a commercial synthesizer (Millitech, PLS-10-A-001) and signal generator (Rohde Schwarz, SMF100A) measured with two different spans of 4 MHz and 80 MHz. Compared to the Millitech synthesizer, the EM-Wise synthesizer shows slightly higher phase noise as shown in figure 2(a) and ±10 MHz side peaks around the main 15 GHz signal as shown in figure 2(b). Note that the side peaks are produced by the 10 MHz reference signal used for phase locking. However, the side peaks can be neglected since the powers are at least 50 dB lower than the main signal power, and the EM-Wise synthesizer has advantages in the output frequency range and step ($f = 14.5-16.0$ GHz with 10 MHz steps for the Millitech synthesizer) at a low cost. Figure 2(c) shows the output powers over the output frequency range of five MIR synthesizers, indicating that the output power flatness is less than 3 dB. The output powers are attenuated to the level of 0−5 dBm, which is the recommended input power range to the multiplier for safety reason.

2.2. New detector array for enhanced sensitivity

One of the essential parts of the millimeter-wave imaging diagnostics such as MIR and electron cyclotron emission imaging (ECEI) system [16] is the vertically aligned detector array. Each detector receives the reflected beams from a poloidally localized area of the plasma cut-off layers through the imaging optics. Until 2013, the KSTAR MIR system had utilized an old 16-channel detector array with a single large hemispherical substrate lens, which was also used for the first proof-of-principle system on the TEXTOR tokamak [17, 18]. In 2014, it was replaced by a different type of detector array with mini-lens array, which is also being used for ECEI. The new detector array consists of a pair of 12-channel mini-lens array and a pair of antenna/detector array boards [19]. Note that each array is used for 12 odd channels or 12 even channels and the KSTAR MIR system uses 16 channels among total 24 channels. Individual mini-lens (characterized by one-inch diameter, elliptical shape at the front surface, and flat one at the rear surface) focuses the collimated beam onto the the detection element, Schottky diode embedded in the dual-dipole antenna [20]. This structure provides enhanced sensitivity and improved optical quality, and the latter will be discussed in section 2.4.

After the 2016 KSTAR campaign, the new antenna/detector array boards (version 2-1) were replaced by modified ones (version 2-2). Here, the version 2-2 is based on a modified dual-dipole antenna matching to a new diode (Virginia Diodes, Inc., W-band Single Anode) because the old diode is not available now and its size and specifications are different from those of the new diode. The test revealed that the sensitivity is similar or slightly improved compared to the version 2-1 as shown in figure 3. The sensitivity of the version 2-2 was enhanced by ∼5 dB at low intermediate frequency (IF). Note that the balun, which determines the IF bandwidth of the array board, was also modified for the version 2-2.

Four IFs from the detector array and the reference mixer are 1.0, 2.8, 4.6, and 6.4 GHz (see figure 4). The power levels of the IF signals from the detector array are typically low as ∼−40 dBm so they are amplified by the low-noise amplifier (Ciao Wireless, CA08-3011 with a typical gain of ∼35 dB and noise figure of ∼2.2 dB). The amplified IF signals are delivered to the electronic system through the 20 m long low-loss broadband cables (Teledyne Storm Microwave, True Blue 290). Because the broadband cable is too rigid and heavy to be directly connected to the detector array and electronic system, two-feet low-loss semi-rigid cables are attached at both ends of the broadband cable. The total loss of the broadband cable and two semi-rigid cables is ∼3.5 dB at 1.0 GHz and ∼10 dB at 6.4 GHz.

2.3. New electronic system for the increased radial channels and bandwidth expansion

Due to the increased radial channels, the previous electronic system with 64 output channels had to be replaced by a new system with 128 output channels (=4 radial channels × 16 poloidal channels × inphase and quadrature (IQ) signals per channel). The basic structure is the same with that of the previous version except the number of frequency channels. Four IF signals delivered through a single broadband cable are split into four different routes according to the frequency by a diplexer. Each IF signal is filtered by a band-pass filter with a bandwidth, which is sufficiently narrow (except IF4) to block undesirable signals generated by inter-modulation between the main peaks and their sub- and higher-harmonics of the probing and LO signals at the array detector and the

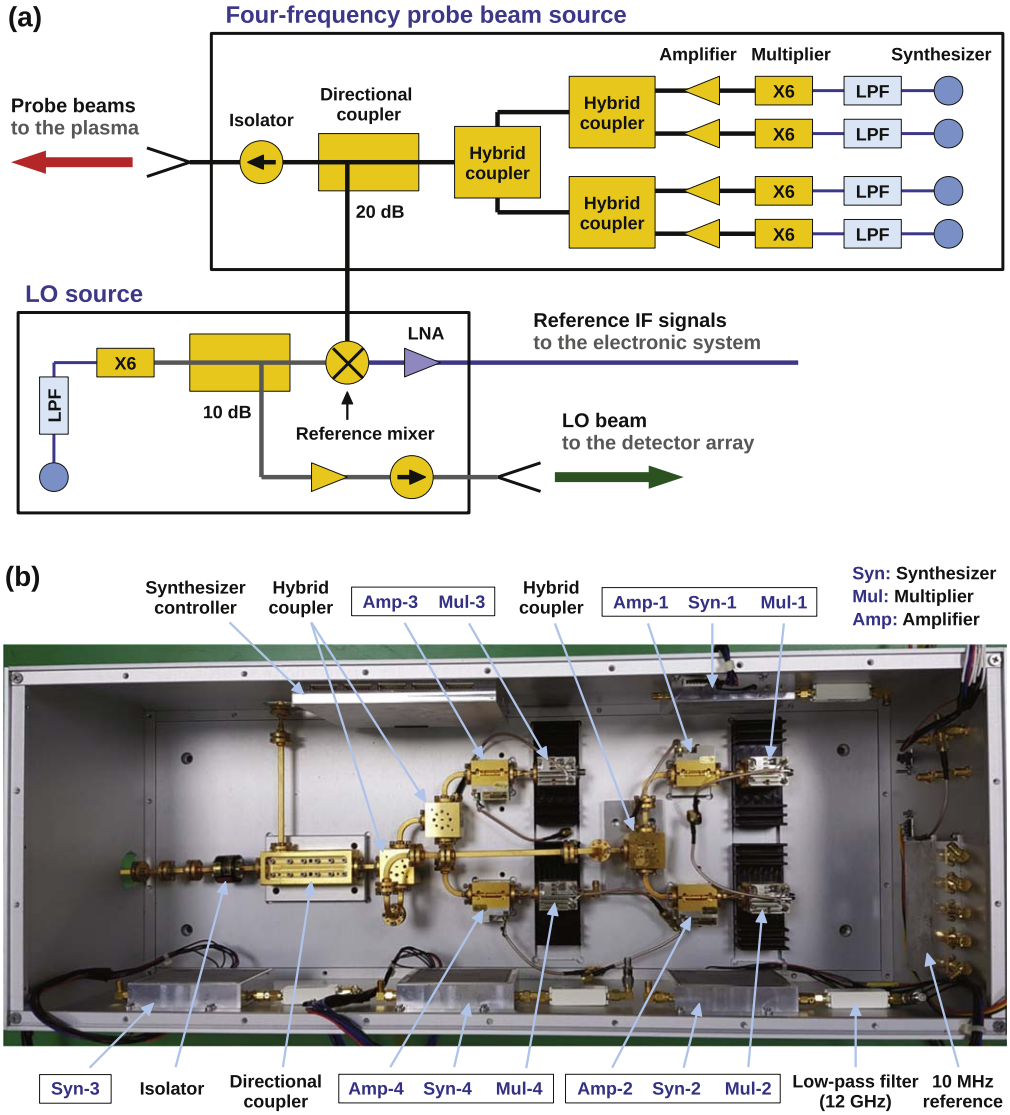

Figure 1. (a) Schematic layout of the four-frequency probe beam source and LO source for the KSTAR MIR system and (b) a view of the probe beam source.

reference mixer. Figure 4 illustrates the IF output spectrum from the reference mixer and overlaid pass-band for each IF peak. Note that the bandwidth of the bandpass filter (for 10 dB attenuation) is 60, 100, 180, and 960 MHz, respectively. The filtered IF signal is mixed with the corresponding reference IF signal and then down-converted to IQ signals by IQ demodulator.

The IQ signals, containing information of density fluctuations near the cut-off layer, are filtered by a low-pass filter. The pass-band was changed several times: ~1.5 MHz in 2014, ~0.5 MHz in 2015, and ~1.9 MHz from 2016. Note that the pass-band of the previous electronic system was ~1 MHz. The upper limit of the poloidal wavenumber of the density fluctuations (k_θ) detectable by the upgraded (and old) MIR system is expected to be ~3.5 cm^{-1} (see section 2.4) and the peak effective poloidal velocity of the fluctuations (v_θ) in fast rotating plasmas reaches up to ~30 km s^{-1}. The dominant term of the effective poloidal velocity is the poloidal projection of the plasma toroidal rotation velocity (U_ϕ), which is given by [3, 21]

$$v_\theta \sim U_\phi \tan\alpha, \tag{1}$$

where α is the magnetic field pitch angle. Figure 5(a) shows the radial profiles of U_ϕ from the charge exchange recombination spectroscopy (CES), α from EFIT reconstruction, and v_θ for a low-field and high-current H-mode discharge heated by 4.4 MW NBI (shot #18674 with the magnetic field $B_0 = 1.8$ T and plasma current $I_p = 700$ kA). The peak effective poloidal velocity is ~33 km s^{-1} and the expected maximum frequency of the mode with $k_\theta = 3.5$ cm^{-1} is ~1.8 MHz from a simple relationship [4]

$$2\pi f \approx k_\theta v_\theta. \tag{2}$$

Therefore, the bandwidth of the IQ signals needs to be expanded to ~2 MHz. Figure 5(b) shows the measured bandwidth of ~1.9 MHz for 10 dB attenuation.

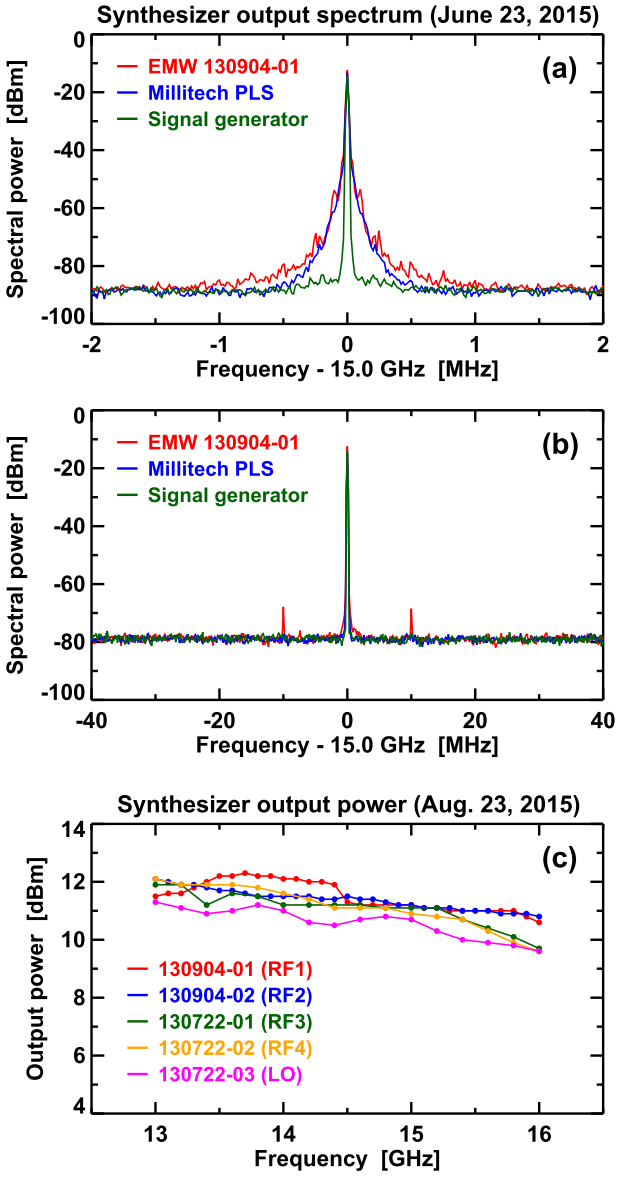

Figure 2. 15 GHz output spectra of the MIR synthesizer (from EM-Wise) compared to those of a commercial synthesizer (from Millitech) and signal generator. These were measured with different spans: (a) 4 and (b) 80 MHz. (c) The output powers over the output frequency range of five MIR synthesizers.

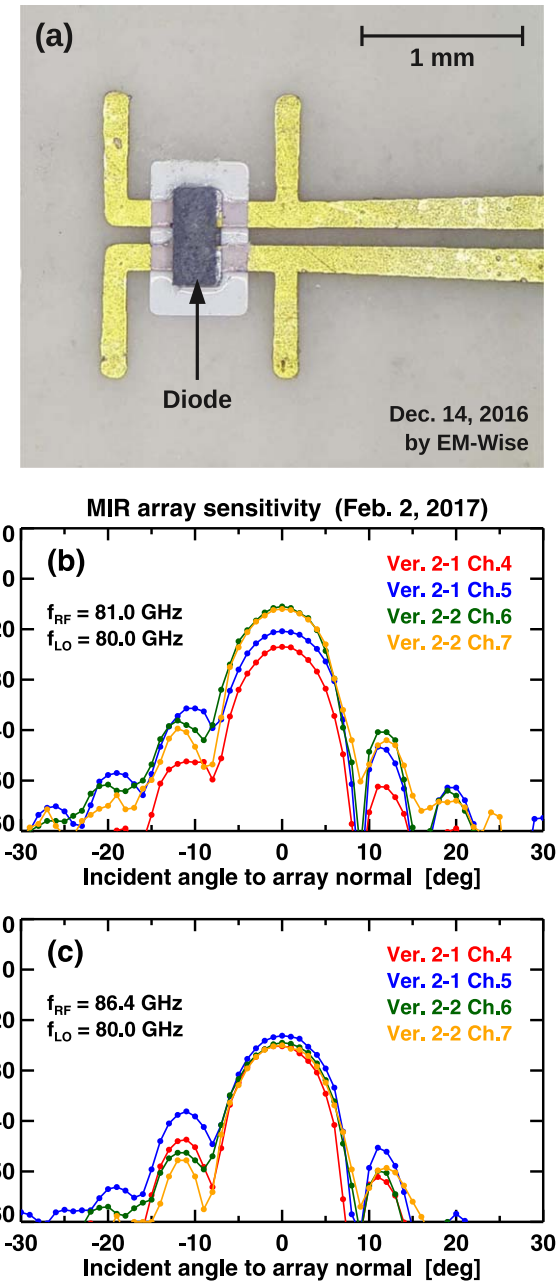

Figure 3. (a) A close-up view of the new dual-dipole antenna (version 2-2 used from 2017). Comparison of the sensitivity between the version 2-1 (used from 2014 to 2016) and the version 2-2 for two IFs: (b) 1.0 GHz and (c) 6.4 GHz. The incident angles of RF and LO beams were simultaneously changed from $-30°$ to $+30°$ with respect to the array normal in the horizontal direction.

The maximum sampling rate of digitizers (D-tAcq, ACQ132PCI-32-02C-LFP) were increased from 2 to 4 MS s^{-1} for the expanded bandwidth of the electronic system, meaning that the highest temporal resolution was improved from 0.5 to 0.25 μs. However, the sampling rate has been often set to 1 or 2 MS s^{-1} for 10 or 5 s data acquisition for slowly rotating plasmas due to the limited memory size of the digitizer. The acquisition time at the maximum sampling rate is only 2.5 s. Thus, we have tried data acquisition with a burst mode to take data for a longer time at high sampling rates from 2016. For instance, the density fluctuations for an H-mode discharge (#19244) were recorded for 4.5 s at 4 MS s^{-1} with the burst mode, in which the digitizers took data for first half of each second. Figure 6 shows the time evolutions of plasma parameters and spectrogram of the MIR IQ signals (RF2—Ch.8) measured with the burst mode. The measurement location with RF2 of 80.8 GHz was changed due to variation of the electron density profile: intermediate radius in the L-mode phase ($t = 0.9-1.4$ s), slightly inside the pedestal top ($t = 1.9-2.4$ s and $2.9-3.4$ s), and in the pedestal ($t = 3.9-4.4$ s).

2.4. New optical system for the new detector array

The MIR optical system consists of two parts: one for transmitting the probe beams (referred to as the transmitter

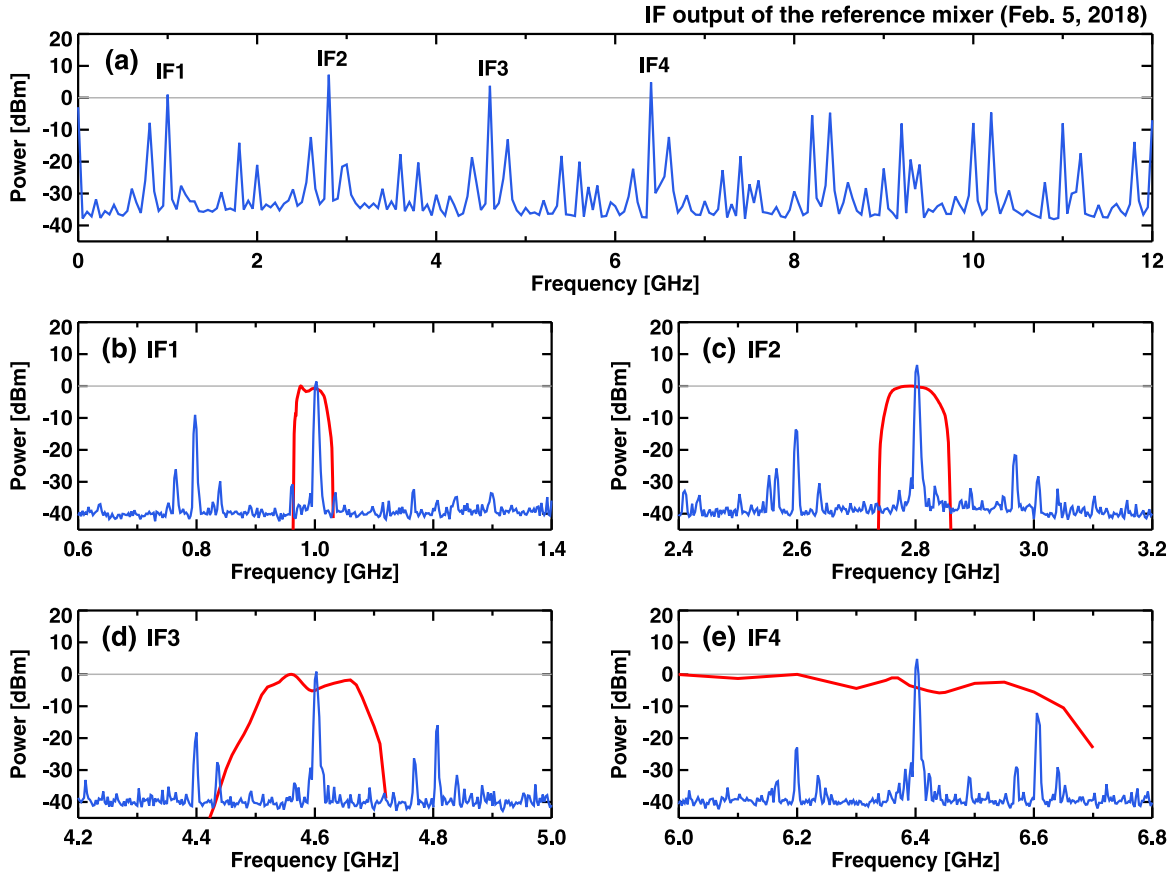

Figure 4. (a) Spectrum of four IF signals from the reference mixer through a low-noise amplifier. Note that four RF frequencies were 87.0, 88.8, 90.6, and 92.4 GHz, and the LO frequency was 86.0 GHz in this test. (b)–(e) Spectrum around each IF signal. Here, the passband for each IF signal in the electronic system (red curve) is overlaid.

optics) and the other for receiving the reflected beams from the cut-off layers (referred to as the receiver optics). The receiver optics was also redesigned since the old detector array was replaced by the entirely different type. The main difference between the old and new receiver optics (from the 2015 campaign) is the significantly reduced zoom factor, which is defined as the ratio of the object height (at the plasma cut-off layer) to the image height (at the detector array). Typical object heights for the two optical systems are similar since the primary measurement target is ion-gyroscale turbulence. The vertical space between adjacent channels at the plasma cut-off layers is ∼5.9 mm for the old receiver optics and ∼6.4 mm for the new receiver optics at the axial location corresponding to the plasma location of $r/a \sim 0.9$, where the normalized radius r/a will be explained in section 3.1. Note that the vertical space can vary depending on the radial measurement location and the coverage with the 16 channels is 10−13 cm. On the other hand, the image heights are completely different since the center-to-center space between adjacent antennas (and mini-lenses) is 2.3 mm for the old array [17] and 14.0 mm for the new array. Thus, the zoom factors are ∼2.6 and ∼0.46, respectively. Note that the first receiver optics for the new array used in 2014 had a large zoom factor of ∼0.93 corresponding to the vertical space of ∼13 mm at the cut-off layer, which is not suitable for the measurement of turbulence, and consequently it was replaced by the new one with the smaller zoom factor in 2015. Figure 7 shows the MIR system with the new optical system.

The usage of mini-lens instead of a large substrate lens in front of individual antenna/detector provides another advantage, which is improved optical quality. Figure 8 shows the response curves of the old and new array detectors through the old and new receiver optics, respectively, for a point source (widely spreading beam source) vertically moved at the axial location corresponding to $r/a \sim 0.9$. The response curves of the new system (new detector array and receiver optics) are more like Gaussian patterns with considerably reduced side lobes compared to those of the old system. The average FWHM of 10 response curves of the center channels (from 4 to 13) is ∼9.1 mm for the old system and ∼9.3 mm for the new system. Note that numbering of the channel was from the top to the bottom for the old array whereas it was reversed for the new array for the consistency with the KSTAR ECEI system. When the spatial resolution is defined based on FWHM of the response curves, which can be regarded as the minimum spot size in the vertical or poloidal direction ($a_{\min}$), the maximum poloidal wavenumber of the detectable fluctuations would be ∼3.5 cm^{-1} for both sets from a relationship $k_{\theta,\max} = 2\pi/\lambda_{\min} = 2\pi/(2a_{\min})$.

The radial measurement location can be flexibly changed from the plasma core to the outboard edge in-between discharges by remotely controlling the probing frequencies or

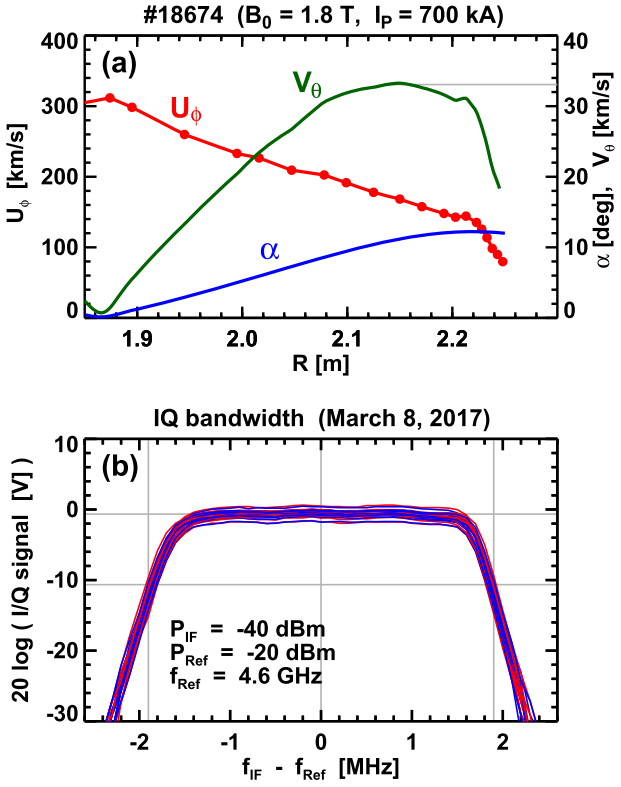

Figure 5. (a) Radial profiles of the toroidal rotation velocity U_ϕ, magnetic field pitch angle α, and effective poloidal velocity of fluctuations v_θ ($\sim U_\phi \tan\alpha$) for a low-field and high-current H-mode discharge heated by 4.4 MW NBI (shot #18674 in 2017). The effective poloidal velocity reaches up to ~33 km s^{-1} and the expected maximum frequency of detectable fluctuations is ~1.8 MHz. (b) Measured bandwidths of the 16 IQ signals for IF3 of 4.6 GHz from the electronic system. The red and blue curves indicate inphase and quadrature signals, respectively. The bandwidth is ~1.9 MHz for 10 dB attenuation.

changing the magnetic field together with remote positioning of three movable lenses. The radial space between adjacent radial channels (with the fixed probing frequency interval of 1.8 GHz) can vary substantially depending primarily on the electron density profile but the nominal space for typical L-mode density profiles is ~2−3 cm.

3. Analysis of the density fluctuations measured with the upgraded MIR

3.1. An L-mode discharge

Density fluctuations were measured with the upgraded MIR system in an L-mode discharge (shot #18332 in 2017), which was a limiter plasma with the magnetic field of 2.2 T and plasma current of 600 kA. The major radius was $R_0 = 1.79$ m and the outer (inner) minor radius was $a = 0.46$ m ($a_i = 0.52$ m). Figure 9(a) shows the time traces of plasma parameters for the discharge. In order to increase the electron temperature (T_e) in the core region, 0.8 MW ECH was applied at $R \sim 1.58$ m (or $r/a_i \sim -0.40$ where $r = R - R_0$) from $t = 2$ s. Indeed, the core electron temperature from the electron cyclotron emission radiometer is increased from ~1.0 keV to ~1.6 keV while the core ion temperature (T_i) of 0.9 keV from the CES is almost unchanged. The line-averaged electron density from the 300 GHz interferometer is slightly increased from 2.4×10^{19} m^{-3} to 2.6×10^{19} m^{-3}. The local electron densities (n_e) were measured with the Thomson scattering system, and the core electron density is slightly decreased from $\sim 3.6 \times 10^{19}$ m^{-3} to $\sim 3.2 \times 10^{19}$ m^{-3} by ECH whereas the electron density at an intermediate radius ($R = 2.04$ m or $r/a = 0.56$) is slightly increased from $\sim 2.3 \times 10^{19}$ m^{-3} to $\sim 2.7 \times 10^{19}$ m^{-3}. The direction of the core toroidal rotation from the CES is changed from counter-current direction (counter-clockwise when viewed from the top) to co-current direction by ECH. The rotation reversal to the co-current direction may be explained by reduced collisionality [22, 23]. The normalized collisionality at the anchor (or stagnation) point ($R \sim 2.10$ m or $r/a \sim 0.67$) is reduced from 0.72 to 0.49 mostly due to the increased electron temperature by ECH. Here, the normalized collisionality is defined as $\nu^* \equiv 0.001\ 18\ qR\ Z_{\rm eff}\ n_e T_e^{-2} \epsilon^{-1.5}$ [24], where q is the safety factor, $Z_{\rm eff}$ is the effective ion charge (assumed 2.0), and $\epsilon = r/R$ is the inverse aspect ratio. Note that the ion temperature and toroidal rotation velocity were measured when neutral beam blip was applied. In order to minimize perturbation to the plasma, short (10 ms ON per second) and low-power (0.8 MW) blip was used.

3.2. Spectral analysis of the measured density fluctuations

Figures 9(b)–(d) show the MIR IQ signals of the radial channel 4 (innermost channel) and poloidal channel 9, spectrogram of the IQ signals, and spectra at four different times for the L-mode discharge. The spectrum at $t_0 = -0.05$ s (before the discharge) shows the MIR system noise property. At $t_1 = 0.95$ s (low-density ohmic phase), a QCM with the peak frequency of ~85 kHz is observed at $R \sim 1.88$ m (or $r/a \sim 0.20$) but the mode looks as if it disappears as the density (and collisionality) increases ($t_2 = 1.4$ s). The suppression by the increased density/collisionality is a typical property of QCM [8, 10–14]. However, since the cut-off layer is moved from $R \sim 1.88$ m to $R \sim 1.99$ m (or $r/a \sim 0.44$) by the increased density, it is not yet clear from the single-channel measurement result whether the QCM is suppressed by the increased collisionality or the measurement location is moved away from the region in which the QCM is unstable. At $t_3 = 3.4$ s (ECH phase), the QCM is not observable at $R \sim 2.02$ m (or $r/a \sim 0.51$). Figures 10(a) and (b) show the electron density profiles at the three distinct times (t_1, t_2, and t_3) and the corresponding X-mode cut-off frequency profiles, respectively. The cut-off layer locations in the midplane of four probing frequencies from 79.0 to 84.4 GHz are indicated by the filled symbols. Figure 10(c) illustrates the locations of all MIR channels on the equilibrium magnetic flux surfaces at the high-density ohmic phase (t_2) reconstructed by EFIT calculation.

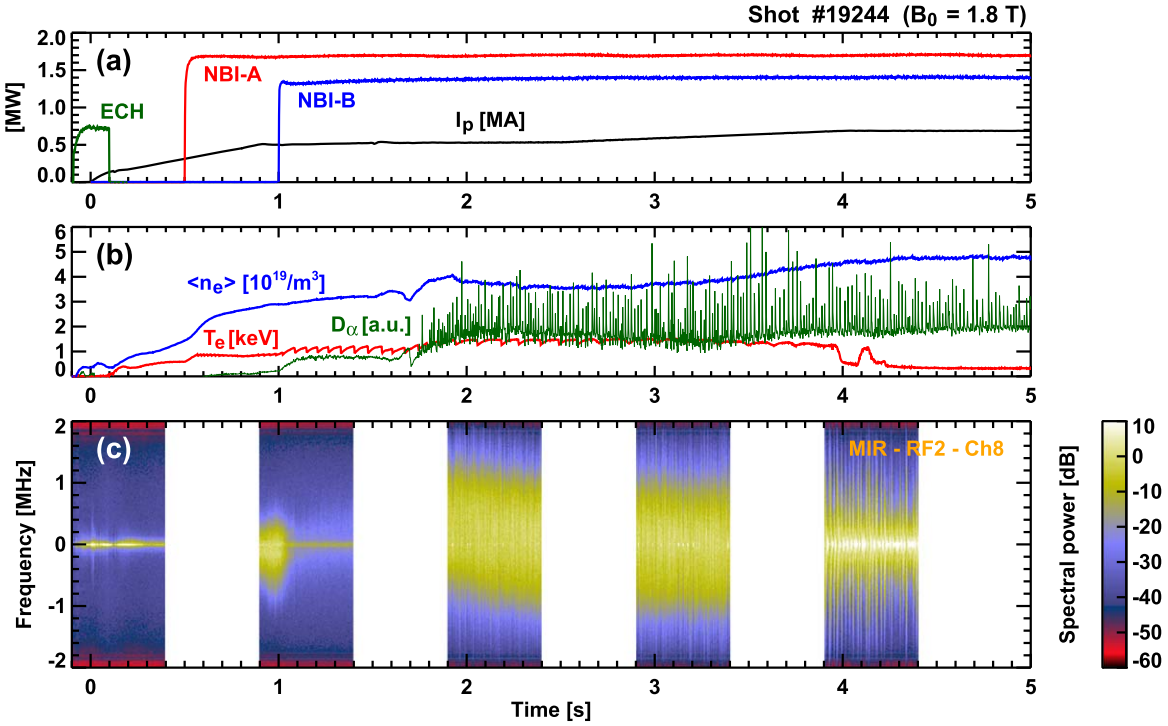

Figure 6. (a) Time evolutions of the plasma current I_p, two NBI powers, and ECH power for an H-mode discharge (shot #19244 in 2017). (b) The electron temperature T_e near the plasma center ($R = 1.81$ m), line-averaged electron density $\langle n_e \rangle$, and D_α emission from the divertor. (c) Spectrogram of the IQ signals of the radial channel 2 and poloidal channel 8 recorded at the maximum sampling rate of 4 MS s^{-1} with a burst mode.

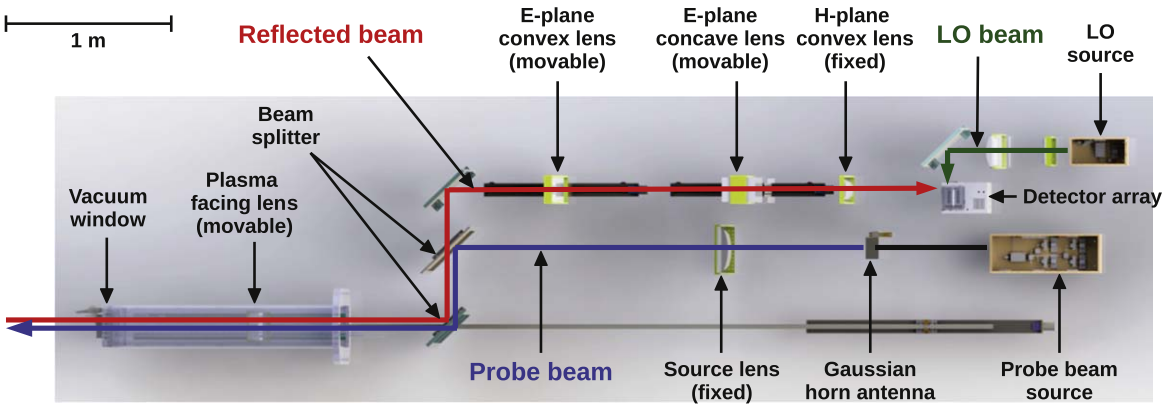

Figure 7. Drawing of the MIR system (top view) with the new optical system utilized from the 2015 campaign.

3.3. The beam blip effect on the plasma rotation and MIR spectrum

Although short low-power beam blips were applied in this discharge, the plasma toroidal rotation was slightly affected by the blips and this can be identified from the MIR spectrogram in figure 9(c). As discussed in section 2.3, the frequency of a mode or broadband turbulence is affected by its rotation velocity (equation (2)), which is influenced by plasma rotation velocity (equation (1)). The spectrum width in the ohmic phase is slightly reduced at 1.5 s when the beam blip is injected, whereas the width in the ECH phase is slightly expanded at 2.5, 3.5, and 4.5 s. Since neutral beam in KSTAR always provides a torque to the plasma in the clockwise direction (or the co-current direction in this discharge), the reduced spectrum width in the ohmic phase indicates a reduced rotation speed in the counter-current direction by the blip and the expanded width in the ECH phase indicates an increased rotation speed in the co-current direction.

The more apparent effect of the beam blips can be found from the MIR spectrogram for an ohmic discharge #16124 ($B_0 = 2.5$ T and $I_p = 800$ kA) with a higher blip power of 1.2 MW as shown in figures 11(a)–(c). The simultaneously measured core toroidal rotation velocities with the CES and x-ray imaging crystal spectroscopy (XICS) demonstrate the beam blip effect on the plasma toroidal rotation. And the spectrogram overlaid with the calculated mode frequency

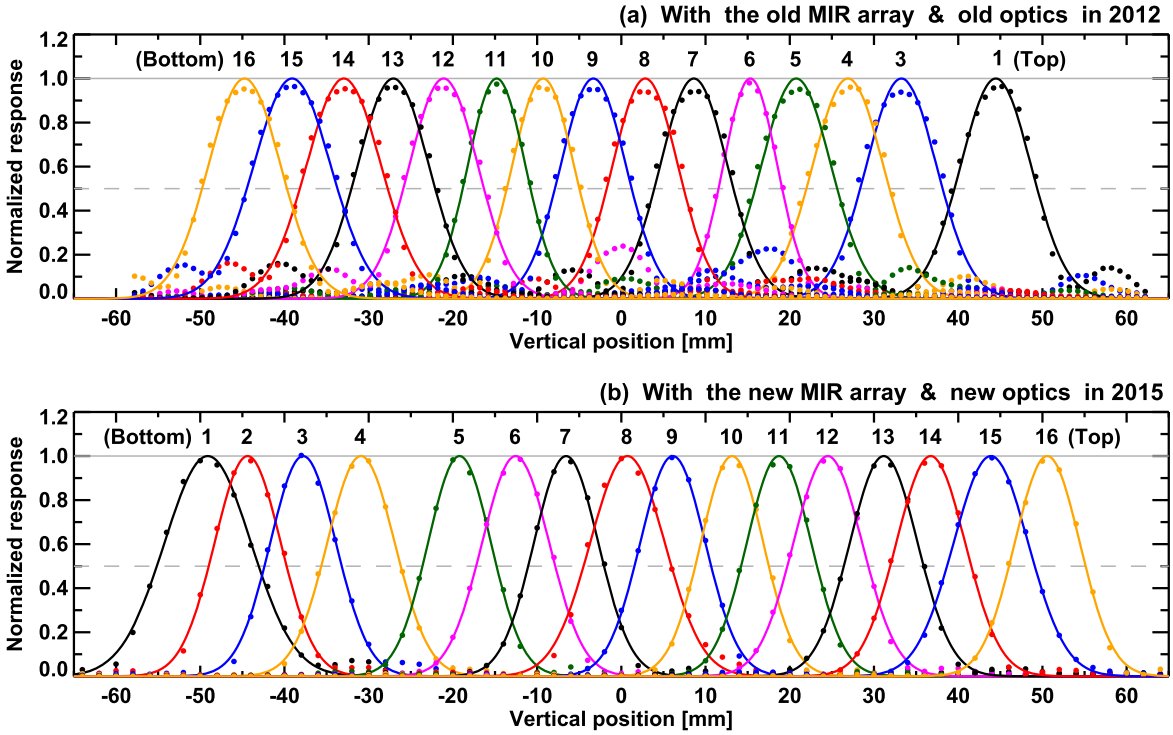

Figure 8. Normalized response curves of the (a) old and (b) new MIR array detectors with the old and new receiver optics, respectively, for a point source vertically moved at an axial location corresponding to the plasma location of $r/a \sim 0.9$. The symbols are the measured responses and the lines are the fitted Gaussian curves. Note that the diode for the channel 2 of the old array was dead, and the channel of the new array corresponding to the MIR channel 4 was dead so the MIR channels from 1 to 4 were shifted to the next channels. Numbering of the channel was from the top to the bottom for the old array whereas it was reversed for the new array for the consistency with the KSTAR ECEI system. (a) Reproduced courtesy of IAEA. Figure from [2]. Copyright 2014 IAEA.

using the toroidal rotation velocity from the XICS and equations (1) and (2), reveals the plasma rotation effect on the frequency of a QCM. The MIR measurement location is $R \sim 1.95$ m ($r/a \sim 0.4$) until ~4.5 s (and then moved outwards due to increased density by gas puffing), and the magnetic pitch angle is ~6.8° at this location. It is assumed for the mode frequency calculation that the poloidal wavenumber of the QCM is 1.8 cm^{-1}. The higher-power blips clearly reduce both the toroidal rotation speed in the counter-current direction and QCM frequency. Note that the QCM in the discharge #16124 was investigated in reference [15]. In figures 11(d)–(f), it is found that the MIR spectrum width is reduced in the ohmic phase and slightly expanded in the ECH phase by the low-power beam blips. Although there was no XICS measurement for the discharge #18332, one can expect that this might be due to the reduced rotation speed in the counter-current direction in the ohmic phase and the slightly increased speed in the co-current direction in the ECH phase.

3.4. Coherence analysis with multiple poloidal channels

Further analysis of the fluctuations for the three phases (t_1, t_2, and t_3) in figure 9(d) has been carried out by applying a coherence analysis to multiple poloidal channels. Figure 12 shows the power spectra of a single channel (RF4—Ch.9), cross-coherence spectra of the poloidal channels from 9 to 11 with respect to the channel 7, and poloidal wavenumber spectra of the channels for the three phases. At the low-density ohmic phase (t_1), the QCM of ~85 kHz is clearly observed in both the power and cross-coherence spectra, and its poloidal wavenumber is ~1.9 cm^{-1}. The effect poloidal rotation velocity of the mode is ~2.8 km s^{-1} in the electron diamagnetic direction, and the rotation direction is well explained by the toroidal rotation direction in the counter-current direction. At the high-density ohmic phase (t_2), the QCM appears to be suppressed by the increased density in the power spectrum as already mentioned in section 3.2, but the mode is observed in the coherence spectra. The poloidal wavenumber of the mode is increased to ~2.4 cm^{-1} and this might cause the increased peak frequency of ~105 kHz even though the effective poloidal rotation velocity is slightly reduced to ~2.7 km s^{-1} (in the electron direction). At the ECH phase (t_3), the QCM appears to be entirely suppressed in the power spectrum but is still observed in the coherence spectra although the peak frequency (to ~30 kHz) and coherence level are substantially reduced. The mode poloidal wavenumber is ~1.7 cm^{-1} and the effective poloidal rotation velocity is ~−1.1 km s^{-1} in the ion direction, which is explained again by the toroidal rotation direction in the co-current direction.

The discrepancy between the power and cross-coherence spectra, which was also reported in the [11], may be explained by different lifetimes between QCM and broadband fluctuations [6]. QCM has a lifetime longer than the time delay between two separated channels, whereas broadband fluctuations are low-correlated and thus have a shorter lifetime than the time delay. Note that the lifetime of fluctuations is often characterized by decorrelation time.

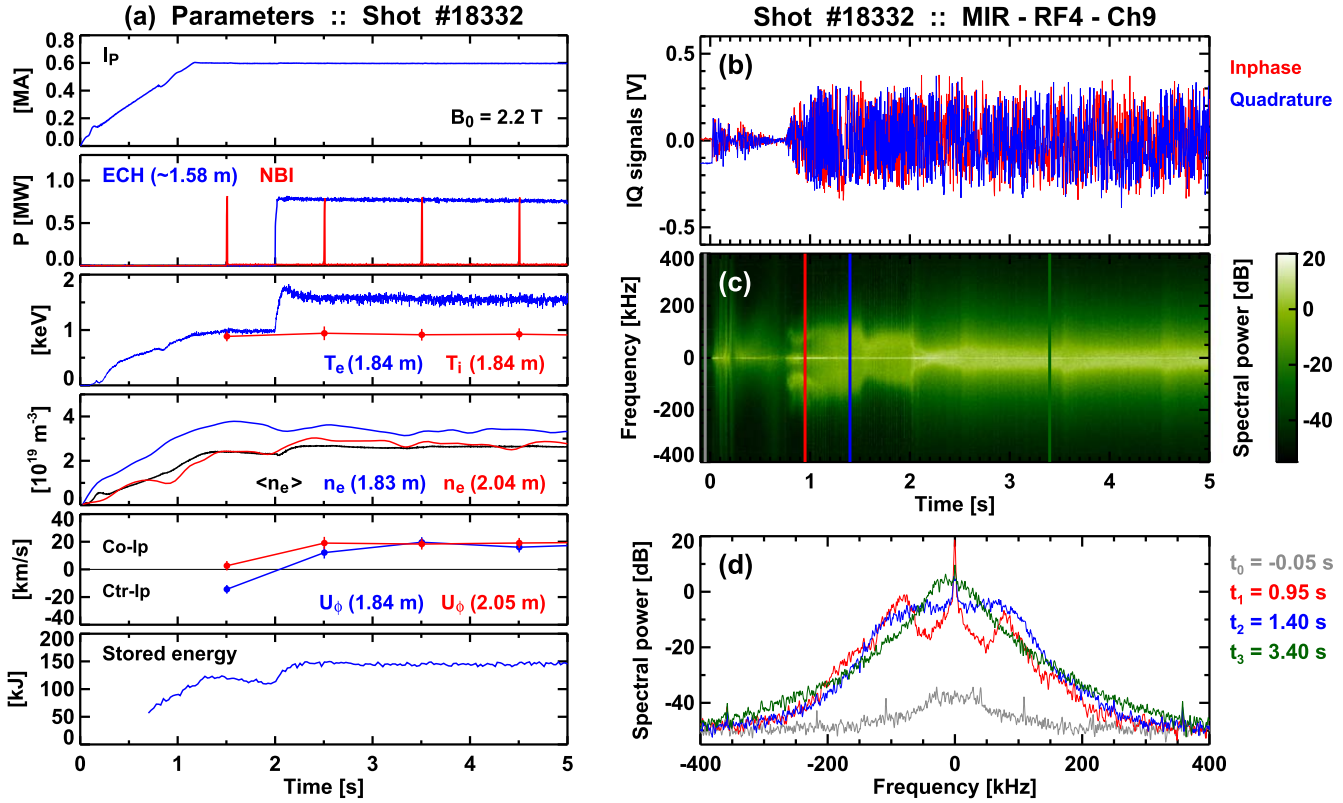

Figure 9. (a) Time traces of the plasma parameters for an L-mode discharge (shot #18332 in 2017): the plasma current I_p, powers of neutral beam blip (10 ms ON per second) and 140 GHz ECH (injected at $R \sim 1.58$ m and $Z \sim 0$ m), electron temperature T_e and ion temperatures T_i at $R = 1.84$ m, line-averaged electron density $\langle n_e \rangle$ and local electron densities n_e at $R = 1.83$ m and 2.04 m, toroidal flow velocities U_ϕ at $R = 1.84$ and 2.05 m, and stored energy. (b) The MIR IQ signals of the radial channel 4 and poloidal channel 9, and (c) the spectrogram of the IQ signals. (d) Spectra at four different times: $t_0 = -0.05$ s (before the discharge showing the system noise), $t_1 = 0.95$ s (low-density ohmic phase), $t_2 = 1.4$ s (high-density ohmic phase), and $t_3 = 3.4$ s (ECH phase).

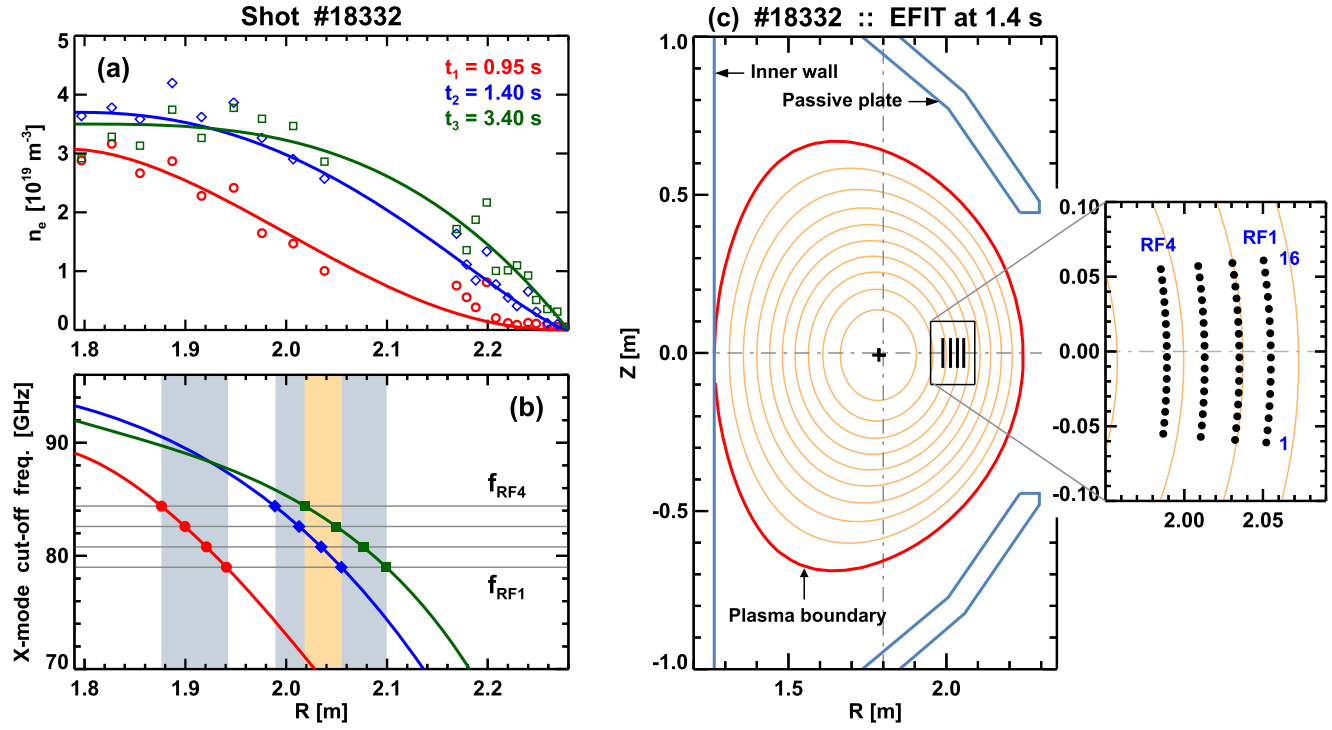

Figure 10. (a) Electron density profiles at three distinct times (t_1, t_2, and t_3) for the discharge #18332. The open symbols indicate the measured profiles with the Thomson scattering system and the solid curves are the fitted ones. (b) The X-mode cut-off frequency profiles corresponding to the fitted density profiles. The cut-off layer locations of four probing frequencies from 79.0 to 84.4 GHz in the midplane are indicated by the filled symbols. (c) Spatial locations of all MIR channels on the equilibrium magnetic flux surfaces at t_2 reconstructed by EFIT.

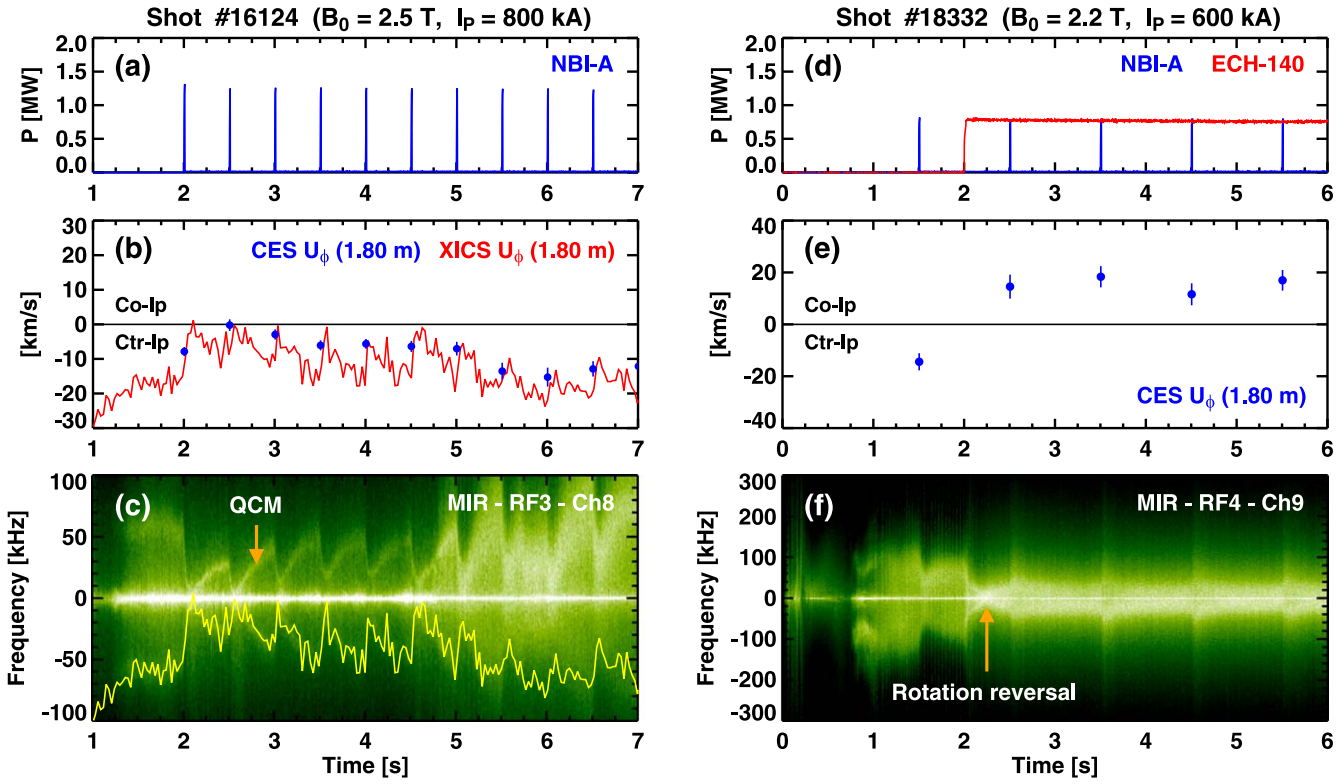

Figure 11. Time traces of (a), (d) the neutral beam blip and (b), (e) core toroidal rotation velocity (at $R = 1.80$ m) from the CES and XICS for two discharges #16124 and #18332. (c), (f) MIR spectrograms. The spectrogram for shot #16124 is overlaid with the calculated mode frequency using the toroidal rotation velocity from the XICS and equations (1) and (2). The MIR measurement location for shot #16124 is $R \sim 1.95$ m until ~4.5 s and then moved outwards due to increased density by gas puffing.

3.5. Analysis with multiple radial channels

Analysis of the fluctuations from multiple radial channels would provide the radial location of the QCM. In figure 13, the QCM is observed at four radii from $R \sim 1.88$ m to ~1.94 m (or $r/a \sim 0.20-0.34$) at the low-density ohmic phase (t_1) from the cross-coherence spectra. The QCM is clear and strong at the inner radius of $R \sim 1.88$ m. At the high-density phase (t_2), the QCM is observable at two or three inner radii ($R \sim 1.99-2.04$ m or $r/a \sim 0.44-0.53$) with reduced coherence from $R \sim 2.04$ m. Based on this measurement, the location of the QCM is $R < 2.04$ m. The measurement for the same discharge with higher probing frequencies would further specify the mode location.

Comparing the cross-coherence spectrum of RF4 (at $R \sim 2.02$ m) at the ECH phase (t_3) in figure 12(f) and that of RF3 (at the similar radius) at the high-density ohmic phase (t_2) in figure 13(f) (blue curve), the amplitude of the QCM is clearly reduced after the ECH power is applied. At this position, the electron temperature gradient (R/L_{Te}) and T_e/T_i are increased by ECH, whereas the electron density gradient (R/L_{ne}), toroidal rotation shear (γ_ϕ), and normalized collisionality are reduced. Here, the normalized gradient is defined as $R/L_X \equiv (R/X)|\mathrm{d}X/\mathrm{d}r|$ and the toroidal rotation shear as $\gamma_\phi \equiv R_0\ \mathrm{d}(U_\phi/R)/\mathrm{d}r$. The radial profiles of the parameters at the two phases are shown in figure 14, and the parameters and their gradients at $R = 2.02$ m are listed in table 1. These profile changes may support that the QCM in this discharge was driven by the electron density gradient rather than the electron temperature gradient or T_e/T_i. Note that the driving parameter for the QCMs induced by ECH seemed to be the promptly increased T_e/T_i (and decreased collisionality) by ECH [15].

3.6. Dependence of the QCM on three parameters

In order to study the QCM property further for the discharge #18332, normalized poloidal coherence length (L_θ/ρ_s) has been calculated as a QCM amplitude and its dependence on three QCM-related parameters (R/L_{ne}, R/L_{Te}, and T_e/T_i) has been investigated, where ρ_s is the ion gyroradius at electron temperature. Figure 15 shows an example of the poloidal coherence length calculation and dependence on the three parameters. The poloidal coherence length was determined as the $1/e^2$-width of the fitted Gaussian curve for each frequency, and the mean value of the coherence lengths at positive and negative peak frequency was chosen for each case. Note that the QCM was not identified in the outer region ($R \gtrsim 2.04$ m) at the high-density ohmic phase and ECH phase, and thus the coherence length was not calculated in this case. The normalized coherence length is weakly dependent on the electron density gradient as already discussed in the previous section 3.5. The relations with the electron temperature gradient and T_e/T_i are not clear. For more clear conclusion, discharges at various plasma conditions will be analyzed in the future.

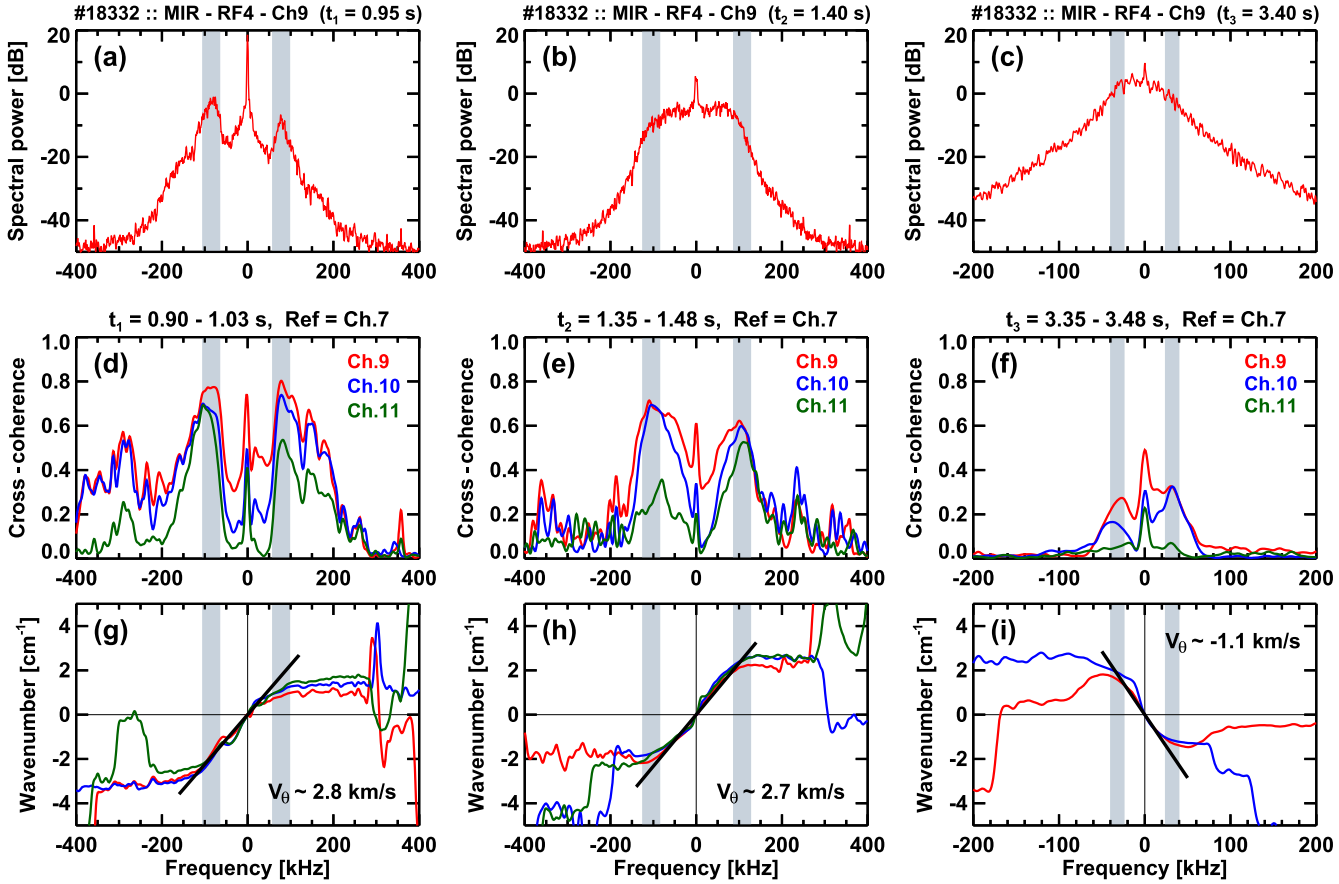

Figure 12. (a)–(c) Power spectra of the MIR IQ signals from a single channel (RF4—Ch.9) at the three phases (t_1, t_2, and t_3) for the discharge #18332. (d)–(f) Cross-coherence spectra of the poloidal channels from 9 to 11 with respect to the channel 7 at the three phases. (g)–(i) Poloidal wavenumber spectra (or dispersion relations) obtained from cross-phase spectra. The black thick line is a fitted line in a low-frequency range providing the mean effective poloidal rotation velocity of fluctuations. Note that the positive (or negative) velocity indicates the rotation in the electron (or ion) diamagnetic direction.

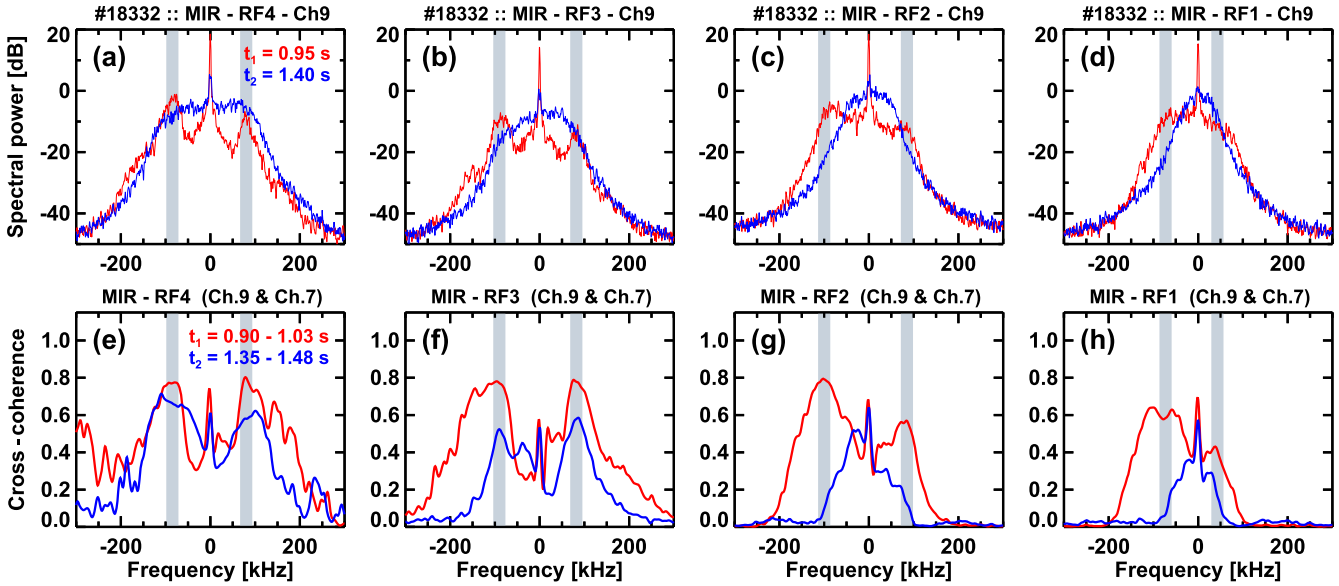

Figure 13. Power spectra and cross-coherence spectra from the four radial channels for the discharge #18332 at two ohmic phases: t_1 (red) and t_2 (blue). The measurement range with the four radial channels is $R \sim 1.88-1.94$ m (or $r/a \sim 0.20-0.34$) at t_1 and $R \sim 1.99-2.06$ m (or $r/a \sim 0.44-0.59$) at t_2.

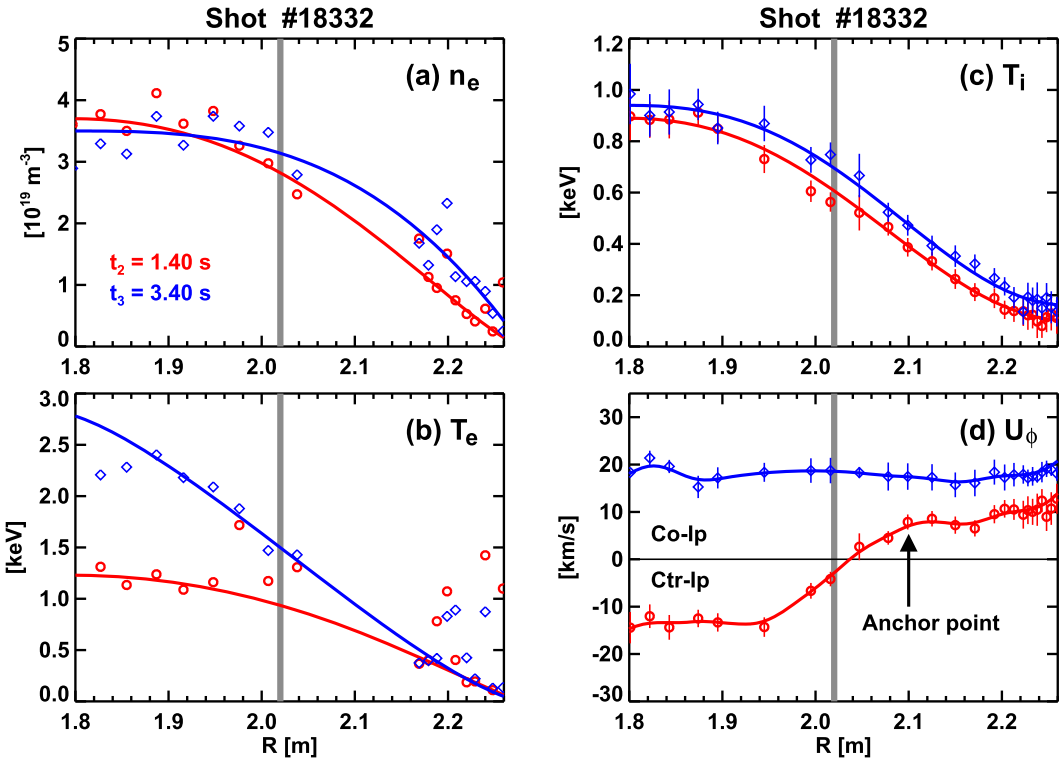

Figure 14. Radial profiles of (a) the electron density, (b) electron temperature, (c) ion temperature, and (d) toroidal rotation velocity for the discharge #18332 at two different phases: high-density ohmic phase (t_2, red circle) and ECH phase (t_3, blue diamond). At $R = 2.02$ m, the electron temperature gradient and T_e/T_i are increased by ECH, whereas the electron density gradient and toroidal rotation shear are reduced. The ion temperature gradient is little changed by ECH. The values of the parameters and their gradients at $R = 2.02$ m are listed in table 1.

Table 1. Plasma parameters and their gradients at $R = 2.02$ m for the discharge #18332 at two different phases: high-density ohmic phase (t_2) and ECH phase (t_3). Here, $R_0 = 1.79$ m, $a = 0.46$ m, and $q(2.02\ \text{m}) = 1.4$. These values were obtained from the profiles in figure 14.

Time	$t_2 = 1.4$ s	$t_3 = 3.4$ s
n_e (10^{19} m^{-3})	2.8	3.1
T_e (keV) (T_e/T_i)	0.94 (1.5)	1.5 (2.2)
T_i (keV)	0.61	0.70
U_ϕ (km s^{-1})	−2.9	19
R/L_{ne} (a/L_{ne})	5.9 (1.4)	3.0 (0.74)
R/L_{Te} (a/L_{Te})	5.7 (1.4)	9.3 (2.3)
R/L_{Ti} (a/L_{Ti})	8.4 (2.0)	7.2 (1.7)
γ_ϕ (kHz)	152	15
ν^*	0.57	0.25

4. Summary

The MIR system has been gradually upgraded over three years since 2014. The number of the probing frequencies was increased from two to four and this increase corresponds to doubled radial detection channels. A 16-channel detector array with a single large substrate lens was replaced by a new detector/mini-lens array, and the dual-dipole antenna of the new detector array was further modified to adapt new available diodes. The 64-channel signal-processing electronic system was replaced by a new 128-channel system with an expanded bandwidth from ∼1 to ∼2 MHz, and the maximum sampling rate of digitizers was increased from 2 to 4 MS s^{-1}. The optical system consisting of the transmitter optics and receiver optics was modified to match the replaced detector array, and the optical quality was improved.

Density fluctuations measured with the upgraded MIR system for an L-mode discharge have been analyzed. Spectrogram of IQ signals from a single channel shows that a QCM of ∼85 kHz appears in the low-density ohmic phase and it is suppressed in the high-density ohmic and ECH phases. This result is consistent with the previous studies on QCM. However, cross-coherence analysis with multiple poloidal channels shows that the QCM remains unsuppressed in the high-density ohmic and ECH phases with varied peak frequency, which may be due to changes in the plasma rotation velocity and poloidal wavenumber of the mode. And the cross-coherence analysis with the multiple radial channels partially provides the radial location of the QCM, which is found to be $R < 2.04$ m. The QCM in this discharge seems to be driven by electron density gradient rather than electron temperature gradient or T_e/T_i. And the poloidal coherence length estimated as a QCM amplitude also shows a weak dependence on the electron density gradient.

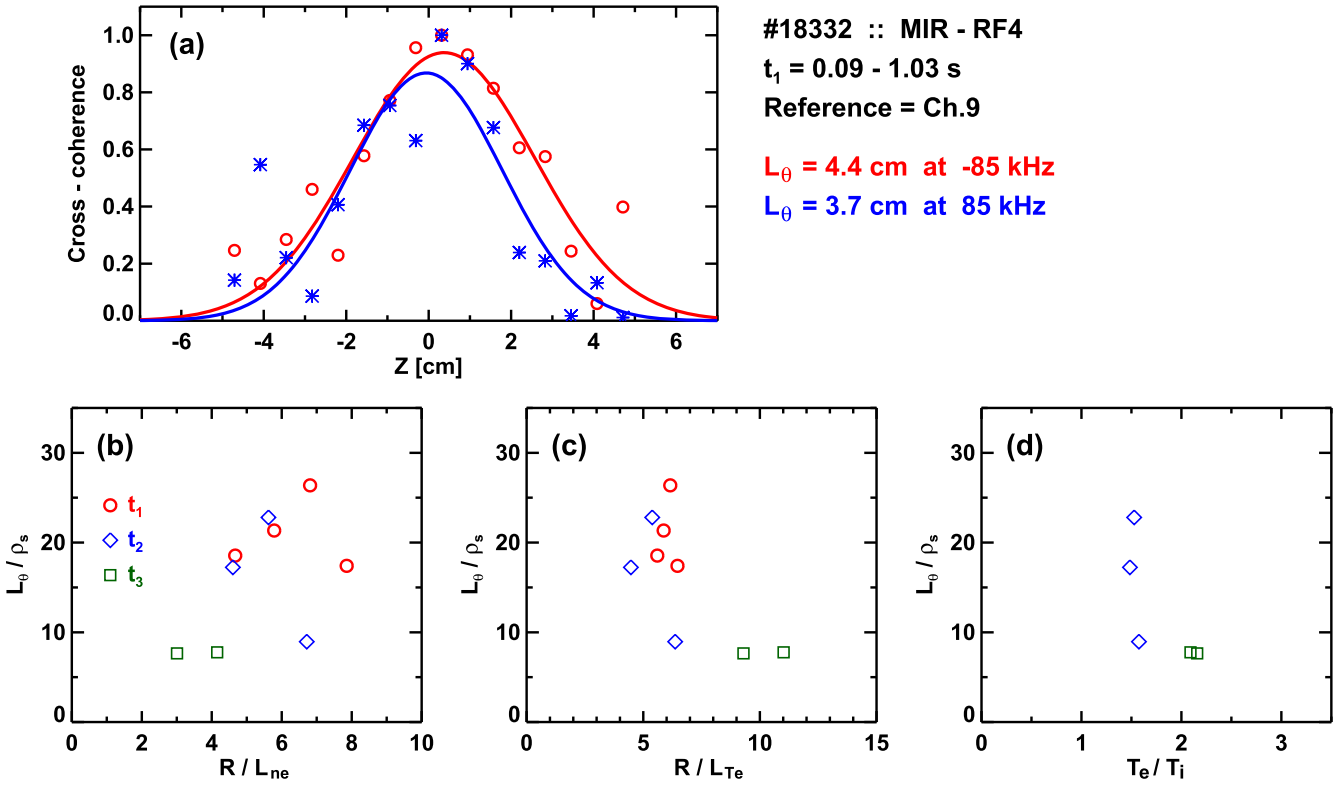

Figure 15. (a) An example of the poloidal coherence length calculation for the discharge #18332. The mean value of the coherence lengths at positive and negative peak frequency of the QCM is chosen for each case. Dependence of the normalized poloidal coherence length L_θ/ρ_s on three parameters: (b) normalized density gradient, (c) normalized electron temperature gradient, and (d) T_e/T_i. Note that the poloidal coherence length was not calculated for the case that the QCM was not identified, and the ion temperature profile was not measured at the low-density ohmic phase (t_1).

Acknowledgments

This research was supported by the Ministry of Science, ICT and Future Planning of Korea under the KSTAR project and the National Research Foundation of Korea under contract Nos. NRF-2014M1A7A1A03029865 and NRF-2017M1A7A1A03064231.

ORCID iDs

W Lee https://orcid.org/0000-0001-6856-3377
M J Choi https://orcid.org/0000-0002-2825-6484
G S Yun https://orcid.org/0000-0002-1880-5865

References

[1] Lee W *et al* 2013 *J. Instrum.* **8** C10018
[2] Lee W *et al* 2014 *Nucl. Fusion* **54** 023012
[3] Lee W *et al* 2016 *Phys. Plasmas* **23** 052510
[4] Lee W *et al* 2016 *Rev. Sci. Instrum.* **87** 11E134
[5] Lee W *et al* 2018 *Nucl. Fusion* **58** 046009
[6] Kramer-Flecken A *et al* 2004 *Nucl. Fusion* **44** 1143
[7] Vershkov V A *et al* 2005 *Nucl. Fusion* **45** S203
[8] Arnichand H *et al* 2014 *Nucl. Fusion* **54** 123017
[9] Kramer-Flecken A *et al* 2015 *New J. Phys.* **17** 073007
[10] Arnichand H *et al* 2015 *Nucl. Fusion* **55** 093021
[11] Arnichand H *et al* 2016 *Plasma Phys. Control. Fusion* **58** 014037
[12] Zhong W L *et al* 2016 *Phys. Plasmas* **23** 060702
[13] Hacquin S *et al* 2016 *Phys. Plasmas* **23** 092303
[14] Citrin J *et al* 2017 *Plasma Phys. Control. Fusion* **59** 064010
[15] Lee J A *et al* 2018 *Phys. Plasmas* **25** 022513
[16] Yun G S *et al* 2014 *Rev. Sci. Instrum.* **85** 11D820
[17] Munsat T *et al* 2003 *Rev. Sci. Instrum.* **74** 1426
[18] Park H *et al* 2003 *Rev. Sci. Instrum.* **74** 4239
[19] Munsat T *et al* 2010 *Appl. Opt.* **49** E20
[20] Zhang P *et al* 2008 *Rev. Sci. Instrum.* **79** 10F103
[21] Ghim Y-C *et al* 2012 *Plasma Phys. Control. Fusion* **54** 095012
[22] Rice J E *et al* 2013 *Nucl. Fusion* **53** 033004
[23] Rice J E 2016 *Plasma Phys. Control. Fusion* **58** 083001
[24] Conway G D *et al* 2006 *Nucl. Fusion* **46** S799